A Bidirectional DC–DC Converter for an Energy Storage System With Galvanic Isolation

Shigenori Inoue, *Member, IEEE*, and Hirofumi Akagi, *Fellow, IEEE*

Abstract—This paper addresses a bidirectional dc-dc converter suitable for an energy storage system with an additional function of galvanic isolation. An energy storage device such as an electric double layer capacitor is directly connected to a dc side of the dc-dc converter without any chopper circuit. Nevertheless, the dc-dc converter can continue operating when the voltage across the energy storage device drops along with its discharge. Theoretical calculation and experimental measurement reveal that power loss and peak current impose limitations on a permissible dc-voltage range. This information may be useful in design of the dc-dc converter. Experimental results verify proper charging and discharging operation obtained from a 200-V, 2.6-kJ laboratory model of the energy storage system. Moreover, the dc-dc converter can charge the capacitor bank from zero to the rated voltage without any external precharging circuit.

Index Terms—Bidirectional isolated dc-dc converter, electric double layer capacitors, energy storage system, loss analysis, starting procedure.

I. INTRODUCTION

GENERALLY, electric power generated by renewable energy sources is unstable in nature, thus producing a bad effect on the utility grid. This fact spurs research on energy storage systems to smooth out active-power flow on the utility grid [1], [2]. Fig. 1 shows a simplified existing energy storage system employing a line-frequency (50- or 60-Hz) transformer, a PWM converter, a bidirectional chopper, and an energy storage device such as electric double layer capacitors (EDLCs) or lithium-ion batteries. The transformer is indispensable for some applications that require voltage matching and/or galvanic isolation between the utility grid and the energy storage device. Replacing the line-frequency transformer with a high-frequency isolated dc-dc converter would make the energy storage system more compact and flexible.

Various bidirectional isolated dc-dc converters have been proposed as the interface to energy storage devices with focus on automotive or fuel cell applications. Most of the presented dc-dc converters have asymmetrical circuit configurations to couple the two dc links having largely different voltages, several tens volts and several hundreds volts [3]–[10].
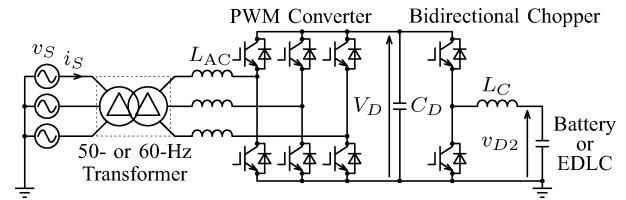
Fig. 1. Existing energy storage system employing a 50- or 60-Hz transformer for voltage matching and/or galvanic isolation.
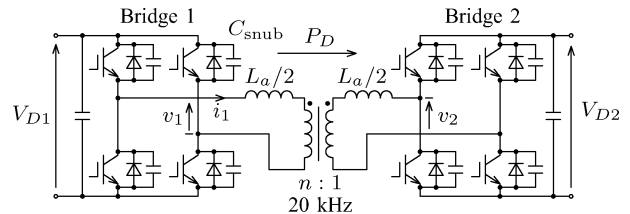

Fig. 2. Bidirectional isolated dc-dc converter.

Fig. 2 depicts a bidirectional isolated dc-dc converter presented in 1991 [11], [12]. It had two symmetrical single-phase voltage-source full-bridge converters. It suffered from a low efficiency because the first-generation IGBTs were used as switching power devices at that time [11]. However, advancement in power device technology over the last decade has enabled the dc-dc converter to operate at an efficiency as high as 97% by using the latest trench-gate IGBTs [13]. A similar dc-dc converter in [14] has also achieved an efficiency of 97%. In addition, the use of silicon-carbide power devices in the near future will raise it to 99%. Therefore, the dc-dc converter in Fig. 2 has become a promising candidate as a power electronic interface for an energy storage system. A bidirectional converter has been discussed to exchange electric power between a fuel cell, a battery, and a load [15], based on a three-port extension of the circuit presented in [11].

Fig. 3 shows the energy storage system using the bidirectional isolated dc-dc converter in Fig. 2. Appropriately choosing the transformer turn ratio n enables to design the voltage rating of the energy storage device, independent of the utility voltage. The energy storage device is directly connected to one of the dc links of the dc-dc converter without any chopper circuit. Nevertheless, the dc-dc converter continues operating even when the voltage across the energy storage device, v_{D2} drops along with its discharge.

However, no paper has addressed the permissible voltage range of v_{D2} in terms of power loss and peak current, and no experimental verification has been confirmed, concerning Fig. 3. This paper analyzes the relationships between the power
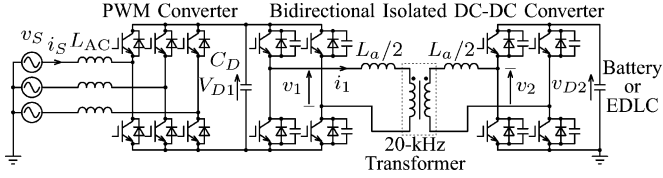
Fig. 3. Alternative energy storage system based on the bidirectional isolated dc-dc converter.
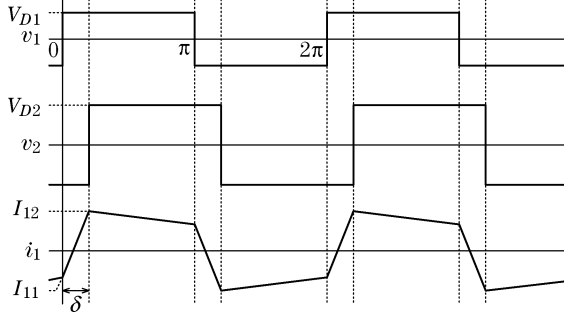

Fig. 4. Simplified theoretical waveforms used to analyze the power losses when $V_{D1} < V_{D2}$.

loss, the peak current, and v_{D2} in a dc-dc converter rated at 10 kW and 20 kHz with V_{D1} fixed to 320 V. Then, the dc-dc converter is designed, constructed, and tested to verify the analysis. A 2.6-kJ energy storage system using an electrolytic capacitor bank, together with the dc-dc converter, demonstrates stable charging and discharging operation. Besides, the dc-dc converter can charge the capacitor bank from zero to the rated voltage without any external precharging or starting-up circuit.

II. THE BIDIRECTIONAL ISOLATED DC–DC CONVERTER

A. Operation Principle and Simplified Theoretical Waveforms

Fig. 4 illustrates simplified theoretical waveforms of the dc-dc converter where $V_{D1} < V_{D2}$. The two single-phase voltage-source full-bridge converters produce square voltages v_1 and v_2. The power transfer P_D can simply be controlled by adjusting the phase shift between v_1 and v_2, δ as expressed by [11]

$$P_D = \frac{V_{D1}V_{D2}}{\omega L}\left(\delta - \frac{\delta^2}{\pi}\right) \tag{1}$$

where $\omega(= 2\pi f)$ is the switching angular frequency of the two single-phase voltage-source full-bridge converters, and L is the sum of the transformer leakage inductance L_{trans} and that of the auxiliary inductors L_a.

As shown in Fig. 4, this paper defines a set of two instantaneous values of the current i_1 as "switching currents," I_{11} and I_{12} which are calculated as

$$I_{11} = -\frac{(V_{D1} + V_{D2})\delta + (V_{D1} - V_{D2})(\pi - \delta)}{2\omega L} \tag{2}$$

and

$$I_{12} = \frac{(V_{D1} + V_{D2})\delta - (V_{D1} - V_{D2})(\pi - \delta)}{2\omega L}. \tag{3}$$

TABLE I
CIRCUIT PARAMETERS OF THE DC–DC CONVERTER

Rated power		10 kW
Rated DC voltage	V_{D1}, V_{D2}	360 V
DC capacitor	C_D	7,100 μF
Unit capacitance constant	H	46 ms
Transformer core material		Finemet FT-3M
Transformer turn ratio	n	1 : 1
Transformer leakage inductance	L_{trans}	1.6 μH (1.6%)
Transformer winding resistance	R_{trans}	17 mΩ (0.13%)
Auxiliary inductor	$L_a/2$	20 μH (19%)
Auxiliary inductor core material		Ferrite (PC44)
Inductor winding resistance	$R_a/2$	20 mΩ (0.15%)
Snubber Capacitor	C_{snub}	0.01 μF (1.6%)
Switching Frequency	f	20 kHz

Based on single-phase 360 V, 10 kW, and 20 kHz.

I_{11} and I_{12} are the instantaneous values of i_1 when v_1 and v_2, respectively, change its polarity from negative to positive.

This paper refers a single-phase voltage-source full-bridge converter as a "bridge." In the following experiments, the transformer turn ratio is unity $(n = 1)$ for the sake of simplicity.

B. Experimental Circuit of the DC–DC Converter

Table I summarizes the circuit parameters of the dc-dc converter. Four auxiliary inductors, totally having $L_a = 40$ μH, are connected in series with the transformer to obtain an inductance of $L = 41.6$ μH together with the leakage inductance of the transformer, $L_{\text{trans}}(= 1.6 \mu\text{H})$.[1] The inductance of 41.6 μH is sufficient to maintain a control resolution of power transfer around 120 W because a time resolution of the controller operated at 20 MHz is 50 ns, corresponding to 0.36° at 20 kHz.

The following sections analyze relationships between power transfer and power losses in the dc-dc converter. The power losses depend not only on the power transfer, but also the dc voltage V_{D2}. When V_{D2} drops along with discharge of the energy storage device, power loss increases at a given power transfer.

III. SNUBBER LOSS

A. Operating Points and ZVS Conditions

In Fig. 2, a snubber capacitor C_{snub} is connected in parallel with each IGBT both to reduce switching loss and to damp out overvoltage. If the IGBT is turned on with its snubber capacitor charged, the IGBT shorts out the snubber capacitor and dissipates the energy stored in the capacitor. This paper refers to this power loss as "snubber loss."

Each IGBT can be turned on in zero-voltage switching (ZVS) manner to generate no snubber loss when both dc voltages are equal $(V_{D1} = V_{D2})$, and the power transfer is sufficient to ensure the ZVS operation. However, when $V_{D1} \neq V_{D2}$, the IGBT is not necessarily turned on in ZVS manner.

[1]Each inductor has an inductance value of $L_a/4 = 10$ μH. Two inductors were connected in series to exhibit $L_a/2 = 20$ μH. Each of two sets of the two series-connected inductors was connected to each side of the transformer. The use of four separated inductors resulted from the authors' previous research where the total inductance had to be adjusted in a range from 10 μH to 40 μH.
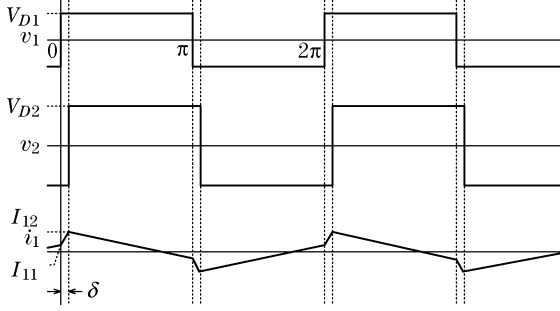
Fig. 5. Waveforms when a positive I_{11} forces bridge 1 to operate in hard-switching manner.

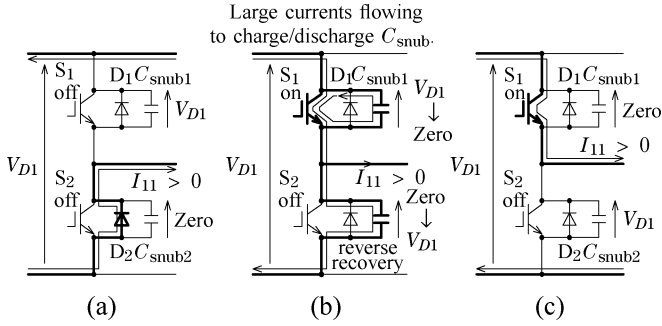Fig. 6. Hard switching on a leg in Bridge 1: (a) just before the dead time ends, (b) rapid charging/discharging of C_{snub1}, and C_{snub2}, (c) after commutation.
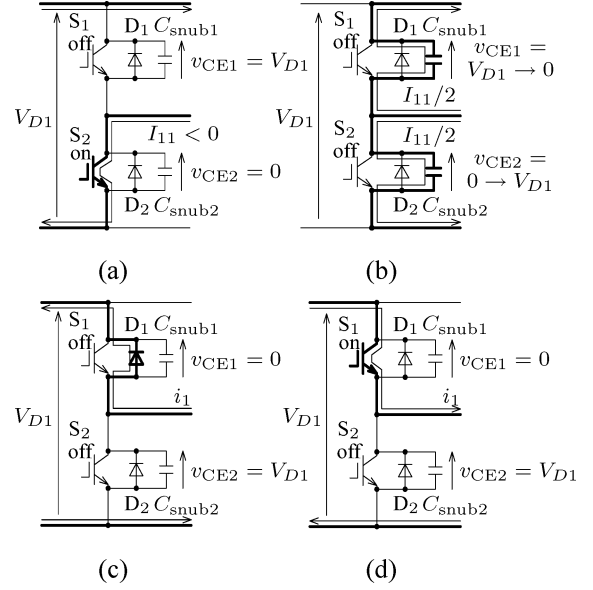

Fig. 7. ZVS on a leg in Bridge 1: (a) just before the dead time starts, (b) just after the dead time starts, (c) diode free wheeling, and (d) current polarity alternates after the dead time.

Fig. 5 shows simplified theoretical waveforms when the IGBTs in bridge 1 are turned on in hard-switching manner. The power transfer is less than that in Fig. 4 although the dc voltages V_{D1} and V_{D2} are the same as those in Fig. 4. The so-called "reverse recovery" occurs in the free-wheeling diodes in bridge 1 because the switching current I_{11} is positive as can be seen in Fig. 5. However, the four IGBTs in bridge 2 are turned on in ZVS manner. One can classify the turn-on processes of the IGBTs in bridges 1 and 2 into the following three: 1) hard switching operation; 2) incomplete ZVS operation; and 3) ZVS operation, depending on the power transfer P_D, the phase shift δ, the dc voltages V_{D1} and V_{D2}, and the dead time. The hard-switching operation and the incomplete ZVS operation can take place only in one bridge, whose dc voltage is lower than the other. The following calculations mainly focus on phenomena in bridge 1 because those in bridge 2 can be described alike.

B. Calculations of the Snubber Loss

1) Hard-Switching Operation: Fig. 6 shows circuit modes when a leg (for example, consisting of S_1 and S_2) operates in hard-switching manner. The IGBTs in bridge 1 are turned on in hard-switching manner if the dc voltage V_{D1} is lower than V_{D2}, and the following equation is satisfied [11]:

$$\delta \leq \frac{V_{D2} - V_{D1}}{2V_{D2}}\pi. \tag{4}$$

The snubber capacitor of S_1, or C_{snub1}, has been charged at V_{D1} [see Fig. 6(a)] before the end of the dead time. Just after S_1 is turned on, D_2 experiences reverse recovery. C_{snub1} discharges from V_{D1} to zero while C_{snub2} charges from zero to

V_{D1} [see Fig. 6(b)]. Only an equivalent resistance of S_1 limits the charging/discharging currents, resulting in a joule loss of $W_{\mathrm{snub}} = C_{\mathrm{snub}}V_{D1}^2$. Note that W_{snub} represents an amount of energy lost at one switching per leg where $C_{\mathrm{snub}} = C_{\mathrm{snub1}} = C_{\mathrm{snub2}}$. Then, the snubber loss P_{snub1} in bridge 1 is calculated as

$$P_{\mathrm{snub1}} = 4W_{\mathrm{snub1}}f = 4C_{\mathrm{snub}}V_{D1}^2 f. \tag{5}$$

2) ZVS Operation: Fig. 7 shows circuit modes when a leg in bridge 1 operates in ZVS manner. Before the dead time, the current of I_{11} is flowing in S_2 [see Fig. 7(a)]. Turning off S_2 starts the dead time. The current flowing in S_2 is commutated to C_{snub1} and C_{snub2}. A resonance begins between the inductance L (see Fig. 2), C_{snub1}, and C_{snub2}. C_{snub1} discharges from V_{D1} to zero while C_{snub2} charges from zero to V_{D1}. Once C_{snub1} discharges down to zero, the current is commutated to D_1 [see Fig. 7(c)]. Providing a gating signal during conduction of D_1 makes S_1 ready to conduct the current. S_1 actually starts to conduct the current in ZVS manner after the current in D_1 decays to zero and alternates its polarity [see Fig. 7(d)]. This operation results in no snubber loss.

3) Incomplete ZVS Operation: The IGBTs in bridge 1 can not necessarily be turned on in ZVS manner even if the switching current I_{11} is negative. Unlike in the ZVS operation, C_{snub1} does not discharge down to zero, and C_{snub2} does not charge up to V_{D1}, if the magnitude of I_{11}, or $|I_{11}|$ is smaller than I_{min}, where

$$I_{\mathrm{min}} = \frac{2\sqrt{V_{D1}V_{D2}}}{Z_r} \tag{6}$$

and

$$Z_r = \sqrt{\frac{L}{C_{\mathrm{snub}}}} \tag{7}$$

as stated in [12]. In this case, the operation of the leg makes a direct transition from Fig. 7(b) to (d), not through (c). Turning on S_1 with the charged snubber capacitor C_{snub1} results in an amount of snubber loss. This paper refers to this as "incomplete ZVS operation."

The following is the calculation of the snubber loss caused by the incomplete ZVS operation. The collector-emitter voltage of S_1, v_{CE1} in Fig. 7(b) can be expressed as

$$v_{\text{CE1}}(t) = \frac{(V_{D1} + V_{D2}) + (V_{D1} - V_{D2})\cos\omega_r t}{2}$$
$$- \frac{Z_r |I_{11}| \sin\omega_r t}{2} \quad (8)$$

where t is the time after the dead time starts, and $\omega_r (= 1/\sqrt{LC_{\text{snub}}})$ is the resonant angular frequency of C_{snub} and L. The collector-emitter voltage $v_{\text{CE1}}(t)$ is not zero at the end of the dead time ($t = T_d$). As a result, the IGBT dissipates an energy of $W_{\text{snub1}} = C_{\text{snub}}\{v_{\text{CE1}}(T_d)\}^2$ when it is turned on. Therefore, the snubber loss P_{snub1} in bridge 1 is calculated as

$$P_{\text{snub1}} = 4fC_{\text{snub}}\{v_{\text{CE1}}(T_d)\}^2. \quad (9)$$

As can be seen in (5) and (9), the snubber loss is proportional to the capacitance of the snubber capacitors. Minimizing the parasitic inductance leads to the use of small snubber capacitors without an excessive overvoltage appearing across an IGBT, thus resulting in reducing the snubber loss.

IV. PROFILE OF THE CURRENT i_1 AND RELATED LOSSES

A. Conducting Loss in the IGBTs

This paper approximates both the on-state voltage across the IGBT, $V_{\text{CE(sat)}}$, and the forward voltage drop across the free-wheeling diode, V_F, to be 1.5 V, that is, $V_{\text{CE(sat)}} = V_F = 1.5$ V, independent of the current flowing in them [13]. The conducting loss in the IGBTs and diodes, P_{cond} can be calculated from the average of the absolute value of the current i_1, or $\langle |i_1| \rangle$.

When either bridge 1 or bridge 2 is operated in hard-switching manner, calculation on Fig. 5 yields:

$$\langle |i_1| \rangle = \frac{1}{\omega L}\left\{ \frac{V_{D1}V_{D2}}{|V_{D1} - V_{D2}|}\frac{\delta^2}{\pi} + |V_{D1} - V_{D2}|\frac{\pi}{4} \right\}. \quad (10)$$

On the other hand, when both bridge 1 and bridge 2 are operated in either ZVS or incomplete ZVS manner, $\langle |i_1| \rangle$ can be calculated from Fig. 4:

$$\langle |i_1| \rangle = \frac{V_{D1}V_{D2}}{\omega L(V_{D1} + V_{D2})}\left\{ -\frac{\delta^2}{\pi} + 2\delta + \frac{(V_{D1} - V_{D2})^2}{V_{D1}V_{D2}}\frac{\pi}{4} \right\}. \quad (11)$$

Both I_{11} and I_{12} have to be obtained first to calculate $\langle |i_1| \rangle$, and then either (10) or (11) should be applied, depending on the switching manner.

B. Copper Loss in the Transformer and the Auxiliary Inductors

Calculation on the waveforms in Figs. 4 and 5 yields the rms value of i_1, or I_1

$$I_1 = \frac{\sqrt{V_{D1}V_{D2}}}{\omega L}\sqrt{-\frac{4}{3\pi}\delta^3 + \delta^2 + \frac{\pi^2}{12}\frac{(V_{D1} - V_{D2})^2}{V_{D1}V_{D2}}} \quad (12)$$

regardless of the switching manner. The copper loss in the transformer and the inductors, P_{copp}, is obtained as

$$P_{\text{copp}} = (R_{\text{trans}} + R_a) \cdot I_1^2 \quad (13)$$

where $R_{\text{trans}}(= 17 \text{ m}\Omega)$ is the winding resistance of the transformer, and $R_a(= 40 \text{ m}\Omega)$ is that of the auxiliary inductors.

C. Core Loss in the Auxiliary Inductors

The four auxiliary inductors were constructed using ferrite (TDK PC44) cores. The effective cross-sectional area of each core was $A_e = 328 \text{ mm}^2$, the effective volume was $V_e = 37.2 \text{ cm}^3$, and the turn number was $N = 6$. An air gap of $g = 1.5$ mm was introduced in the magnetic path. Thus, the instantaneous magnetic flux density b_{ind} is approximately expressed as

$$b_{\text{ind}} \simeq \frac{\mu_0}{g}Ni_1 \quad (14)$$

where μ_0 is the permeability of vacuum. The datasheet of PC44 indicates that its core loss per volume is 600 kW/m^3($= 0.6$ W/cm^3) when the maximum flux density is 200 mT at a frequency of 100 kHz at a temperature of 25 °C.

In a power electronic context, the Steinmetz equation $P_{\text{core}}[\text{W/m}^3] = kf^\alpha B^\beta$ helps well to calculate an amount of core loss in a magnetic material where k is a material constant, f is a frequency of magnetization, and B is the maximum flux density. The exponents, α and β, are not constant values, but depend on f, B, and the waveform of the magnetic flux. When a ferrite core is excited at 20 kHz, the eddy-current loss can be much smaller than the hysteresis loss. Thus, α is assumed to be unity. The other exponent β usually ranges from 2.6 to 2.8. However, this paper takes an approximation of $\beta = 2$ so as to keep the analysis simple. This approximation allows to treat the core loss in the same way as the copper loss.

If the core loss per volume in PC44 can be approximated by mfB^2, the coefficient m is given as 0.15 mW/HzT^2. This paper assumes that a sinusoidal 20-kHz current having an rms value as large as I_1 is responsible for the core loss in the auxiliary inductors. The core loss in the four auxiliary inductors can be calculated as

$$P_{\text{core}}[\text{W}] = 4mf\left(\frac{\mu_0}{g}N\sqrt{2}I_1\right)^2 V_e = \frac{8mf\mu_0^2 N^2 V_e}{g^2}I_1^2 \quad (15)$$

where $\sqrt{2}$ is the coefficient to transform an rms value into an amplitude. Therefore, the core loss in the four auxiliary inductors can be treated as an equivalent winding resistance of

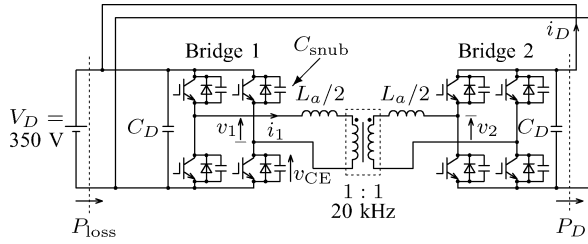$$R_{\text{core(ind)}} = \frac{8mf\mu_0^2 N^2 V_e}{g^2} = 23 \text{ m}\Omega. \quad (16)$$

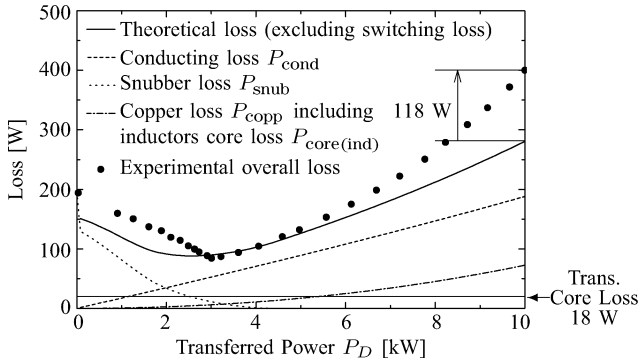Fig. 8. Experimental circuit to measure the power loss of the dc-dc converter.

Fig. 9. Comparison between calculated and experimental power losses at $V_{D1} = V_{D2} = 350$ V.

Fig. 10. Sum of theoretical conducting and snubber losses ($P_{\text{cond}} + P_{\text{snub}}$) when P_D is positive.

This equivalent resistance enables to calculate the core loss in the auxiliary inductors as a part of copper loss. Further detailed analysis, for example, as found in [16], should bring an improvement of accuracy to the core-loss calculation although it is out of the scope of this paper.

V. POWER LOSSES AND LOWER LIMIT OF V_{D2}

A. Comparison Between Theoretical and Experimental Losses

Theoretical losses described in the previous section are compared to measured results on the basis of an experimental dc-dc converter rated at 10 kW and 20 kHz. Fig. 8 shows the experimental circuit to measure the overall loss of the dc-dc converter. The circuit parameters in Fig. 8 are the same as those in Table I. Both theoretical calculation and experimental measurement are carried out under $V_{D1} = V_{D2} = 350$ V.

Note that V_D in Fig. 8 is a dc voltage source. A connection between the two dc links allows the power P_D to be regenerated back to the dc voltage source. Thus, the power coming from V_D equals P_{loss}, that is the overall loss in the dc-dc converter.

Fig. 9 shows comparisons between the theoretical and experimental losses. The solid line corresponds to the theoretical overall loss P_{theory}, although it excludes the switching loss in the IGBTs, or P_{sw}. Even in the ZVS operation, the switching loss is not zero due to the so-called "tail current" in the IGBTs. It requires modeling of the IGBT switching behavior in this dc-dc converter to theoretically predict the switching loss P_{sw}. However, it is beyond the scope of this paper.

When $P_D = 10$ kW, the theoretical losses were obtained as follows. The conducting loss was $P_{\text{cond}} = 189$ W. The snubber loss was $P_{\text{snub}} = 0$ W. The copper loss both in the transformer and the inductors $P_{\text{copp}} = 73$ W including the core loss in the inductors, $P_{\text{core(ind)}}$. The core loss in the transformer was
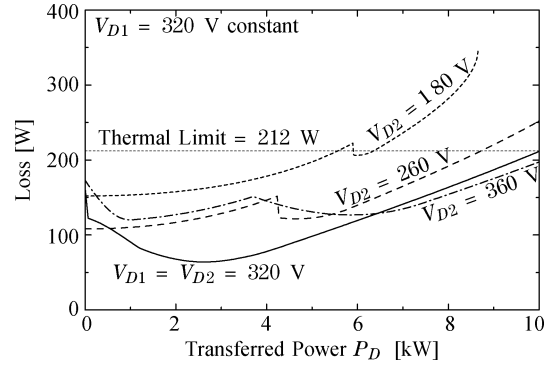
$P_{\text{core(tr)}} = 18$ W, almost independent of the power transfer. Thus, the theoretical overall loss P_{theory} is 282 W.

The experimental results, P_{loss}, on the other hand, was 400 W. Thus, the difference between the theoretical and measured results were 118 W. It would include the switching loss in the IGBTs that was excluded from the theoretical overall loss. In [13], the switching loss in the IGBTs was 90 W when a power of 10 kW was transferred. Although the difference of $118\ \text{W} - 90\ \text{W} = 28$ W can not be identified, the theoretical calculations can be valid because the error of 28 W corresponds to 0.28% of the power transfer of 10 kW, and 7% of the measured overall loss of 400 W.

A 250-V, 5-kW bidirectional isolated dc-dc converter was constructed and tested in [17]. The dc-dc converter employed the third-generation planar-gate IGBTs rated at 600 V and 100 A. The overall loss of the dc-dc converter was measured at six switching frequencies from 10 to 20 kHz with a step of 2 kHz. This measurement enabled to extract the switching loss from the overall loss because the switching loss is proportional to the switching frequency. As a result, the switching loss was approximately 75 W at a power transfer of 5 kW and a switching frequency of 20 kHz. The switching loss of 90 W in the 350-V, 10-kW dc-dc converter in this paper can be a reasonable value, considering the raised voltage from 250 V to 350 V, the increased power from 5 to 10 kW, and the use of the latest trench-gate IGBTs.

B. Thermal Limit and V_{D2}

Fig. 10 shows calculated results of conducting and snubber losses in the IGBTs ($P_{\text{cond}} + P_{\text{snub}}$) when the power transfer P_D is positive. One dc voltage V_{D1} was kept constant at 320 V, while the other dc voltage V_{D2} was changed as a parameter. Achieving the ZVS operation becomes difficult with $V_{D1} \neq V_{D2}$, compared to $V_{D1} = V_{D2} = 320$ V, resulting in an increased snubber loss around $P_D = 3$ kW.

Fig. 10 defines $P_{\text{cond}} + P_{\text{snub}} = 212$ W at $V_{D1} = V_{D2} = 320$ V as a "thermal limit." The losses in the IGBTs, which are the most dominant in the overall loss, may make the IGBT modules mounted on a heatsink suffer from the highest temperature. The temperature of the IGBT modules, more precisely the semiconductor chips in the modules, determines the maximum power transfer. Therefore, this paper considers only the losses in the IGBT modules as the thermal limit.
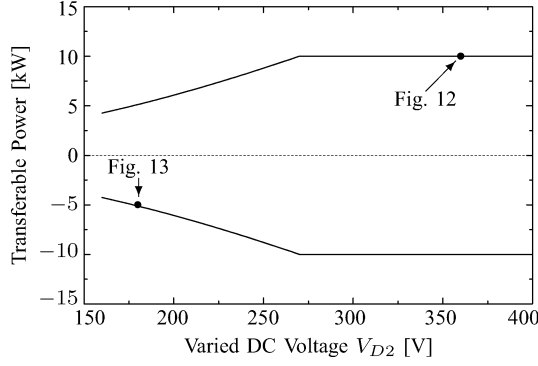
Fig. 11. Transferable powers when the peak value of current i_1 is limited to 60 A, and two operating points in experiments.
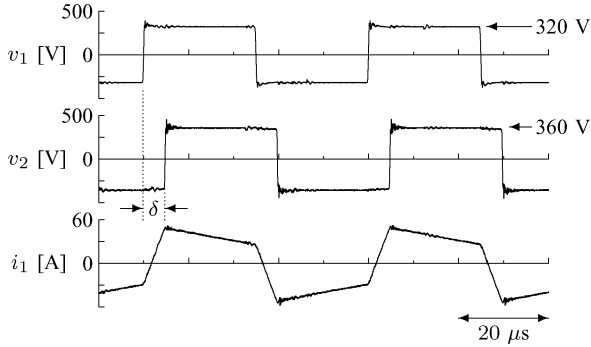

Fig. 12. Experimental waveforms when $V_{D1} = 320$ V, $V_{D2} = 360$ V, $\delta = 35°$, and $P_D = 10$ kW.

When $V_{D2} = 180$ V, the losses in the IGBTs exceed the thermal limit at $P_D > 5.6$ kW. Hence, when $V_{D2} = 180$ V, the dc-dc converter has to operate under 5.6 kW. When $V_{D2} = 260$ V, the losses in the IGBTs exceed the thermal limit at $P_D > 8.6$ kW. Hence, when $V_{D2} = 260$ V, the dc-dc converter has to operate lower than 8.6 kW. Likewise, the dc voltage V_{D2} imposes limitations on maximum power transfer.

VI. PEAK CURRENT IN THE AUXILIARY INDUCTORS

The ferrite cores in the auxiliary inductors would be magnetically saturated if the current i_1 exceeds 60 A because the magnetic flux density reaches 0.3 T as calculated by (14). The dc-dc converter has to be operated considering the limitation on the peak value of i_1, or $I_{1\mathrm{peak}}$. The peak current imposes limitations on the dc voltage V_{D2}. When $V_{D1} > V_{D2}$, the peak current $I_{1\mathrm{peak}}$ equals I_{11}. When $V_{D1} < V_{D2}$, the peak current $I_{1\mathrm{peak}}$ equals I_{12}.

Fig. 11 shows maximum power transfer when the peak current is limited lower than 60 A. Solid dots "•" indicate the operating points of the waveforms shown in Figs. 12 and 13. When $V_{D2} = 180$ V, $I_{1\mathrm{peak}}$ exceeds 60 A at $P_D = 5.1$ kW. When $V_{D2} = 260$ V, $I_{1\mathrm{peak}}$ exceeds 60 A at $P_D = 9.4$ kW. Both the power loss and the peak current impose limitations on the power transfer P_D and the dc voltage V_{D2}. Operation of the dc-dc converter has to satisfy both limitations.

Fig. 12 shows the observed waveforms when one dc voltage is 320 V while the other is 360 V at $P_D = 10$ kW from bridges 1 to 2. Fig. 13 shows another example of the observed waveforms which was taken when $V_{D1} = 320$ V while $V_{D2} = 180$ V at
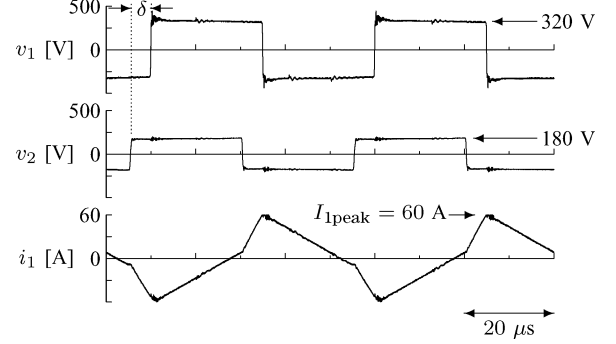

Fig. 13 Experimental waveforms when $V_{D1} = 320$ V, $V_{D2} = 180$ V, $\delta = -41°$, and $P_D = -5$ kW.

$P_D = 5$ kW from bridges 2 to 1. The power transfer P_D was limited below 5 kW, as shown in Fig. 11 when the dc-dc converter had a set of dc voltages of $V_{D1} = 320$ V and $V_{D2} = 180$ V. The peak current $I_{1\mathrm{peak}}$ was 60 A in Fig. 13, as calculated in this section.

VII. APPLICATION TO AN ENERGY STORAGE SYSTEM

A. The 200-V, 10-kW, 2.6-kJ Laboratory Model

Fig. 14 depicts the experimental energy storage system rated at 200 V, 10 kW, and 2.6 kJ. Circuit parameters in the dc-dc converter were the same as those in Table I. An electrolytic capacitor bank C_{ES} of 60,000 μF was used to simulate an EDLC bank. The capacitor bank is charged up to 350 V and discharged down to 190 V. Thus, an energy of 2.6 kJ is stored into, and released out of, the capacitor bank. It corresponds to 70% of the energy stored in C_{ES} at $v_{D2} = 350$ V. The carrier frequency of the PWM converter used as the front end was 10 kHz.

B. Charging and Discharging of the Capacitor Bank

Fig. 15 shows the observed waveforms when the energy storage capacitor bank C_{ES} was repetitively charged up to 350 V, and then discharged down to 190 V. The waveform of i_{D2} was observed via a low-pass filter with a cut-off frequency of 800 Hz. The maximal power transfer was 9.3 kW. In this experiment, the phase shift δ had a square waveform with an amplitude of 30° to make the controller simple. In actual energy storage systems, however, the power transfer P_D should be given by power demand, or a higher level controller regulating the voltage on the utility grid.

VIII. STARTING PROCEDURE

At the starting of the system, an inrush current would flow into the auxiliary inductors L_a and the transformer if bridge 1 produced a square voltage of v_1 at $v_{D1} = 320$ V and $v_{D2} = 0$ V. The inrush current would result in magnetic saturation in the cores of L_a, leading to an even larger inrush current. Hence, this paper presents a special operation mode called "precharging operation" to charge the capacitor bank from zero to the rated voltage of 320 V, preventing such an inrush current from flowing. The precharging operation allows the energy storage system to require no external starting-up or precharging circuit. The precharging operation presented in this paper can be considered as a well-known "soft-start" procedure
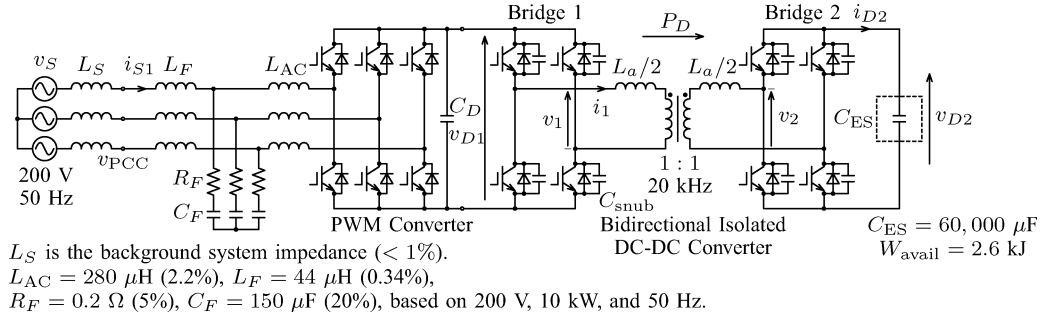
Fig. 14. A 200-V, 10-kW experimental circuit with energy-storage electrolytic capacitors of 60 000-μF to simulate an EDLC bank.
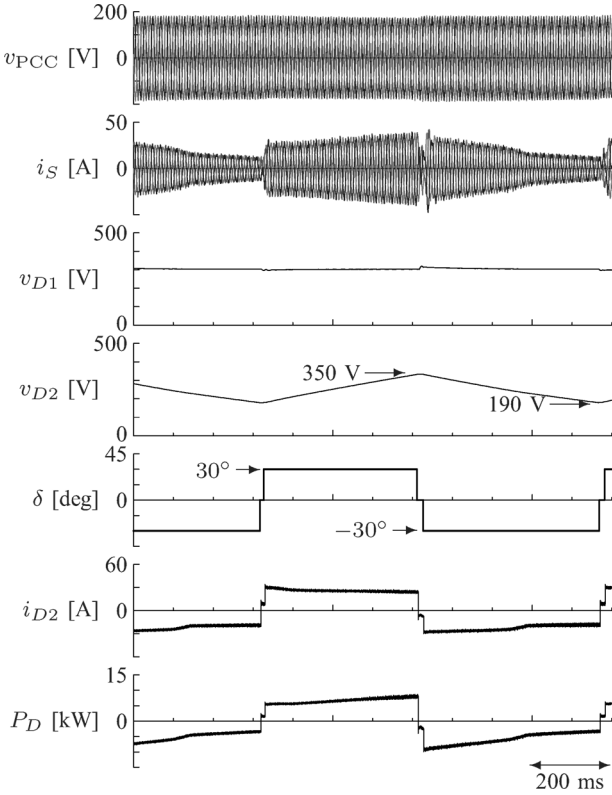

Fig. 15. Experimental waveforms of charging and discharging of the capacitor bank ($W_{\text{avail}} = 2.6\,\text{kJ}$).
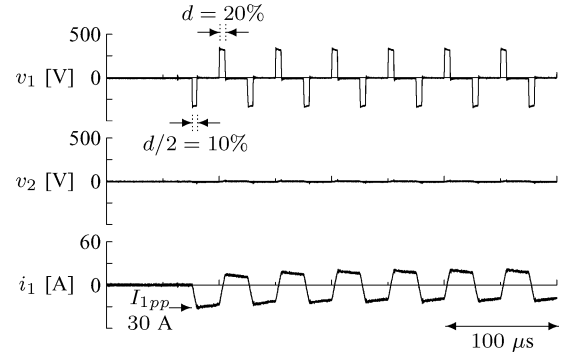

Fig. 16. Transient waveforms when the dc-dc converter starts precharging the capacitor bank.
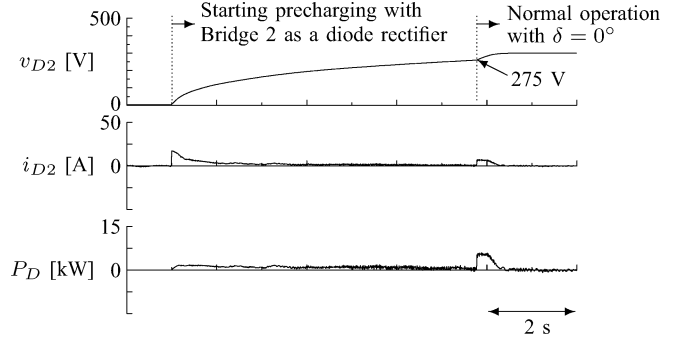

Fig. 17. Experimental waveforms of dc voltage, current, and power in the precharging period.

of dc-dc converters [18]. However, experimental verification of the precharging operation makes a technical contribution to the energy storage system with the large dc capacitor bank.

Fig. 16 shows the starting-up and precharging transient waveforms of the dc-dc converter when the capacitor bank began being charged from 0 to 320 V. In this experiment, v_{D1} had been already charged up to 320 V before the dc-dc converter started the precharging operation. Bridge 1 produced a voltage v_1 with a duty ratio of $d = 20\%$ rather than 100% while bridge 2 was operated as a diode rectifier with all the IGBTs kept off. The first pulse of v_1 had a half duty ratio of $d/2 = 10\%$ to suppress dc magnetization of the transformer. The peak value of i_1 at the first pulse of v_1, I_{1pp} is expressed as

$$I_{1pp} = \frac{\pi V_{D1}}{\omega L} \frac{d}{2}. \tag{17}$$

The negative peak current reached 30 A in Fig. 16 while its theoretical value was 19.2 A.

Fig. 17 shows the experimental waveforms of the dc voltage, current, and power. The starting procedure took approximately 8 s to charge the capacitor bank from zero to 320 V. No excessive inrush current flowed into the capacitor bank. When the voltage across the capacitor bank, v_{D2} reached 275 V, the dc-dc converter changed its operation mode from the precharging operation to the normal operation with the square voltages of v_1 and v_2 having no phase shift ($d = 100\%$ and $\delta = 0°$). The power transfer P_D in the normal operation at $\delta = 0°$ has a negative-feedback effect to balance the two dc voltages v_{D1} and v_{D2} due to the existence of the dead time. Therefore, v_{D2} was charged up to the same voltage as v_{D1} naturally after v_{D2} reached 275 V.

IX. Conclusion

This paper has addressed a bidirectional isolated dc-dc converter suitable for an energy storage system. Theoretical calculations of power losses and peak current have clarified the dc-voltage limitations in the energy storage system. Experimental results have revealed that the dc-dc converter can charge and discharge the capacitor bank properly. Moreover, the dc-dc converter can charge the capacitor bank from zero to the rated voltage without any external precharging circuit.

References

[1] P. F. Ribeiro, B. K. Johnson, M. L. Crow, A. Arsoy, and Y. Liu, "Energy storage systems for advanced power applications,," *Proc. IEEE*, vol. 89, no. 12, pp. 1744–1756, Dec. 2001.

[2] T. Kinjo, T. Senjyu, N. Urasaki, and H. Fujita, "Output levelling of renewable energy by electric double layer capacitor applied for energy storage system," *IEEE Trans. Energy Convers.*, vol. 21, no. 1, pp. 221–227, Mar. 2006.

[3] M. Jain, M. Daniele, and P. K. Jain, "A bidirectional dc-dc converter topology for low power application," *IEEE Trans. Power Electron.*, vol. 15, no. 4, pp. 595–606, Jul. 2000.

[4] T. Kohama, M. Yamashima, and T. Nishimiya, "Operation-mode control of active-clamped bi-directional flyback converter as EDLC charger and discharger," in *Proc. Power Conversion Conf. (PCC)*, Osaka, Japan, 2002, vol. 3, pp. 1155–1159.

[5] A. D. Swingler and W. G. Dunford, "Development of a bi-directional dc/dc converter for inverter/charger applications with consideration paid to large signal operation and quasi-linear digital control," in *Proc. IEEE Power Electronics Specialists Conf. (PESC)*, 2002, vol. 2, pp. 961–966.

[6] F. Z. Peng, H. Li, G.-J. Su, and J. S. Lawler, "A new ZVS bi-directional dc-dc converter for fuel cell and battery application," *IEEE Trans. Power Electron.*, vol. 19, no. 1, pp. 54–65, Jan. 2004.

[7] L. Zhu, "A novel soft-commutating isolated boost full-bridge ZVS-PWM dc-dc converter for bi-directional high power applications," *IEEE Trans. Power Electron.*, vol. 21, no. 2, pp. 422–429, Mar. 2006.

[8] L. Shi, L. Sun, D. Xu, and M. Chen, "Optimal design and control of 5 kW PWM plus phase-shift (PPS) control bidirectional dc-dc converter," in *Proc. IEEE Appl. Power Electron. Conf. Expo (APEC)*, Dallas, TX, Mar. 2006.

[9] Y. Hu, J. Tatler, and Z. Chen, "A bi-directional dc/dc power electronic converter for an energy storage device in an autonomous power system," in *Proc. Power Electron. Motion Cont. Conf. (IPEMC)*, 2004, vol. 1, pp. 171–176.

[10] H.-J. Chiu and L.-W. Lin, "A bidirectional dc-dc converter for fuel cell electric vehicle driving system," *IEEE Trans. Power Electron.*, vol. 21, no. 4, pp. 950–958, Jul. 2006.

[11] R. W. De Doncker, D. M. Divan, and M. H. Kheraluwala, "A three-phase soft-switched high-power density dc/dc converter for high-power applications," *IEEE Trans. Ind. Appl.*, vol. 27, no. 1, pp. 63–73, Jan./Feb. 1991.

[12] M. H. Kheraluwala, R. W. Gascoigne, D. M. Divan, and E. D. Baumann, "Performance characterization of a high-power dual active bridge dc-to-dc converter," *IEEE Trans. Ind. Appl.*, vol. 28, no. 6, pp. 1294–1301, Nov./Dec. 1992.

[13] S. Inoue and H. Akagi, "A bidirectional isolated dc-dc converter as a core circuit of the next-generation medium-voltage power conversion system," *IEEE Trans. Power Electron.*, vol. 22, no. 2, pp. 535–542, Mar. 2007.

[14] M. Pavlovsky, S. W. H. de Haan, and J. A. Ferreira, "Concept of 50 kW DC/DC converter based on ZVS, quasi-ZCS topology and integrated thermal and electromagnetic design," in *Proc. Eur. Conf. Power Electronics Applications (EPE)*, 2005.

[15] J. L. Duarte, M. Hendrix, and M. G. Simões, "Three-port bidirectional converter for hybrid fuel cell systems," *IEEE Trans. Power Electron.*, vol. 22, no. 2, pp. 480–487, Mar. 2007.

[16] W. A. Roshen, "A practical, accurate and very general core loss model for nonsinusoidal waveforms," *IEEE Trans. Power Electron.*, vol. 22, no. 1, pp. 30–40, Jan. 2007.

[17] S. Inoue and H. Akagi, "Loss analysis of a bi-directional isolated dc/dc converter," in *Proc. Int. Power Electron. Conf. (IPEC)*, 2005.

[18] N. Mohan, T. M. Undeland, and W. P. Robbins, *Power Electronics, Converters, Applications and Design*, 3rd ed. New York: Wiley, 2003, p. 342.

Shigenori Inoue (S'02–M'07) was born in Fujimi, Saitama, Japan, on January 29, 1979. He received the B.S. and M.S. degrees from Tokyo Metropolitan University, Tokyo, Japan, in 2002 and 2004, respectively, and the Ph.D. degree from Tokyo Institute of Technology in 2007.

He is currently a Research Fellow with the Japan Society for Promotion of Science (JSPS). His research interests include medium-voltage power conversion systems, bidirectional isolated dc-dc converters, SiC/GaN-based power devices, and active power filters.

Hirofumi Akagi (M'87–SM'94–F'96) was born in Okayama, Japan, in 1951. He received the B.S. degree from Nagoya Institute of Technology, Nagoya, Japan, in 1974, and the M.S. and Ph.D. degrees from Tokyo Institute of Technology, Tokyo, Japan, in 1976 and 1979, respectively, all in electrical engineering.

In 1979, he joined Nagaoka University of Technology, Nagaoka, Japan, as an Assistant and then Associate Professor in the Department of Electrical Engineering. In 1987, he was a Visiting Scientist at the Massachusetts Institute of Technology (MIT), Cambridge, for ten months. From 1991 to 1999, he was a Professor in the Department of Electrical Engineering, Okayama University, Okayama, Japan. From March to August 1996, he was a Visiting Professor at the University of Wisconsin-Madison and then MIT. Since January 2000, he has been a Professor in the Department of Electrical and Electronic Engineering, Tokyo Institute of Technology. He has published some 70 IEEE Transactions papers and two invited papers in THE PROCEEDINGS OF THE IEEE. He has made presentations many times as a Keynote or Invited Speaker internationally. His research interests include power conversion systems, ac motor drives, high-frequency resonant inverters for induction heating and corona discharge treatment processes, and utility applications of power electronics such as active filters for power conditioning, self-commutated BTB systems, and FACTs devices.

Dr. Akagi received two IEEE Industrial Applications Society (IAS) TRANSACTIONS prize paper awards in 1991 and in 2004, two IEEE Power Electronics Society (PELS) TRANSACTIONS prize paper awards in 1999 and in 2003, nine IEEE IAS Committee prize paper awards, the IEEE William E. Newell Power Electronics Award in 2001, and the IEEE IAS Outstanding Achievement Award in 2004. He was elected as a Distinguished Lecturer of the IEEE Industry Applications and Power Electronics Societies for 1998–1999. He currently is President of the IEEE Power Electronics Society.